

Coherent magnon and acoustic phonon dynamics in tetragonal and rare-earth-doped BiFeO₃ multiferroic thin films

K. I. Doig,¹ F. Aguesse,² A. K. Axelsson,² N. M. Alford,² S. Nawaz,³ V. R. Palkar,³ S. P. P. Jones,¹ R. D. Johnson,¹ R. A. Synowicki,⁴ and J. Lloyd-Hughes^{1,5,*}

¹University of Oxford, Department of Physics, Clarendon Laboratory, Parks Road, Oxford, OX1 3PU, United Kingdom

²Imperial College, Department of Materials, South Kensington Campus, London SW7 2AZ, United Kingdom

³Indian Institute of Technology Bombay, Mumbai 400076, India

⁴J. A. Woollam Co., Inc., 645 M Street, Suite 102, Lincoln, Nebraska 68508 USA

⁵University of Warwick, Department of Physics, Gibbet Hill Road, Coventry, CV4 7AL, United Kingdom

(Received 8 November 2012; revised manuscript received 2 August 2013; published 19 September 2013)

Coherent magnons and acoustic phonons were impulsively excited and probed in thin films of the room temperature multiferroic Bi_{1-x-y}Dy_xLa_yFeO₃ using femtosecond laser pulses. The elastic moduli of rhombohedral, tetragonal, and rare-earth doped BiFeO₃ were determined from acoustic-mode frequencies in conjunction with spectroscopic ellipsometry. A weak ferromagnetic order, induced alternately by magnetization in the growth direction or by tetragonality, created a magnon oscillation at 75 GHz, indicative of a Dzyaloshinskii-Moriya interaction energy of 0.31 meV.

DOI: [10.1103/PhysRevB.88.094425](https://doi.org/10.1103/PhysRevB.88.094425)

PACS number(s): 77.55.Nv, 71.55.Ht, 76.50.+g, 78.47.-p

I. INTRODUCTION

In magnetoelectric multiferroics, the magnetization and electrical polarization are strongly coupled,¹⁻⁴ enabling potential applications in magnetic data storage and spintronic devices.⁵ In addition to their response to static stimuli, dynamic magnetoelectric (ME) coupling under alternating fields is of great interest⁶ because Maxwell's equations permit a linear ME coupling if the electric and magnetic fields vary temporally and spatially.⁷ Recent demonstrations of novel dynamic ME effects include the electric-field control of Raman-active spin modes,⁸ the time-resolved reflectivity of magnons in a hexaferrite,⁹ and the discovery of electric-dipole-active spin waves (electromagnons).¹⁰⁻¹²

Bismuth ferrite (BFO) is one of the few room-temperature multiferroics, and as such has been studied extensively.¹³ In the bulk phase ferroelectricity arises from a rhombohedral distortion to the perovskite structure (Fig. 1): the 6s² lone pair on Bi³⁺ creates a polarization along $\langle 111 \rangle$, with a concomitant tilt of the oxygen octahedra. The *G*-type antiferromagnetic (AFM) order on the 3d⁵ Fe³⁺ sites is disrupted by a weak ferromagnetic component. The Fe-O-Fe chain has no center of symmetry, resulting in the canting of adjacent spins via the Dzyaloshinskii-Moriya (DM) interaction.^{13,14} However, in bulk crystals of BFO a long-range spin cycloid¹⁵ with a wavelength of 64 nm averages the weak ferromagnetic moment to zero.

In contrast to the strong magnetoelectric (ME) coupling observed for multiferroics such as RMnO₃, where polarization stems directly from magnetic order,¹ static ME coupling in BFO is weak. Ferroelectric and AFM orders originate from different ions, and the spin cycloid prohibits the linear ME effect in bulk BFO.¹³ While the application of a large magnetic field (20 T) can suppress the cycloid and recover a linear ME effect,¹⁶ epitaxial strain² and chemical doping^{17,18} have been explored as routes to obtain stronger coupling at lower magnetic fields. The partial substitution of Bi on the perovskite *A*-site with lanthanides has been

explored as a route to enhance the remnant polarization, saturation magnetization, and the coupling between the two orders. Among the lanthanides, Dy³⁺ has a relatively high magnetic moment (electron configuration [Xe]4f⁹), yielding a greater magnetization both in bulk and thin film.¹⁹ La³⁺ is nonmagnetic (electron configuration [Kr]4d¹⁰5s²5p⁶) and lowers the remnant polarization.¹⁹

In this article a study of dynamic ME coupling in BFO thin films is reported, in particular the influence of tetragonality and of lanthanide substitution on the perovskite *A*-site. Impulsive photoexcitation using femtosecond ultraviolet pulses creates a coherent magnon oscillation that is tracked by a time-delayed infrared probe. Strain pulses carried by longitudinal acoustic phonons are utilized to obtain the films' elastic moduli.

Section II outlines the various sample-characterization techniques undertaken. In Sec. II A the crystal structure of the investigated films is reported, while in Sec. II B results from spectroscopic ellipsometry and density functional theory (DFT) are used to discuss the complex refractive index and orbital hybridization. Section III outlines the principle experimental technique of this study, pump-probe reflectivity, and presents the experimental results for pristine samples. Section IV provides a detailed discussion of the observed acoustic phonon modes and discusses the elasticity tensor in anisotropic BFO. The experimental investigation and possible origin of the magnon mode are presented in Sec. V, before concluding remarks are given in Sec. VI.

II. SAMPLE CHARACTERIZATION

A. Growth and x-ray diffraction

Thin films of rhombohedral-like BiFeO₃ (R-BFO), tetragonal BiFeO₃ (T-BFO), Bi_{0.7}Dy_{0.3}FeO₃ (BDFO), and Bi_{0.6}La_{0.1}Dy_{0.3}FeO₃ (BLDFO) were grown on (001)-oriented LaAlO₃ and MgO substrates by pulsed laser deposition.^{17,18} The majority of the results presented herein were obtained for films on LaAlO₃: where important, the substrate used

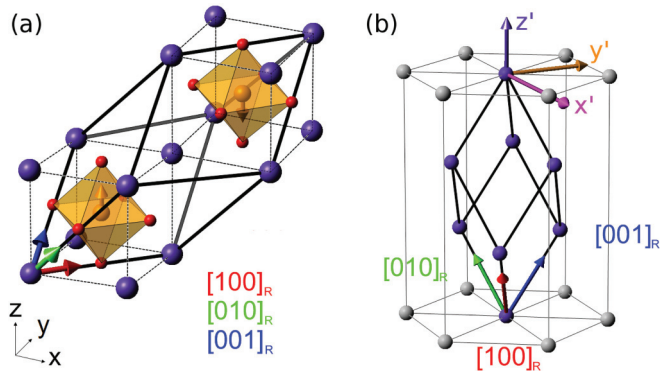


FIG. 1. (Color online) Crystal structure of BiFeO_3 and coordinate systems. (a) Relationship between pseudocubic perovskite structure (thin lines) and rhombohedral unit cell (thick lines). Bismuth, iron, and oxygen atoms are drawn in blue, orange, and red, while orange arrows denote spins. The Cartesian axes x , y , z of the pseudocubic structure and the unit vectors of the rhombohedral cell are also shown. (b) The Cartesian axes x' , y' , z' used to describe the properties of the rhombohedral structure (blue circles, thick lines) are shown along with the alternative trigonal cell (gray circles, thin lines).

is identified with the suffix “/L” or “/M” (e.g., BDFO/M). Film thicknesses were in the range from 290 to 450 nm (from ellipsometry, see below), with a surface roughness of less than 20 nm (from AFM). While monoclinic or tetragonal phases are stabilized by compressive strain on LaAlO_3 for thicknesses below 300 nm, thicker films exhibit strain relaxation towards the bulk rhombohedral phase.²⁰

High-resolution ω - 2θ x-ray diffraction scans and reciprocal space maps were used to examine the crystal structure of our films, using a four-circle x-ray diffractometer (PANalytical X’pert Pro) with a Cu $K\alpha$ source and a monochromator. In Fig. 2(c) the pseudocubic (002) peak of the LaAlO_3 substrate

(space group $R\bar{3}m$, $a = 3.789 \text{ \AA}$, $\alpha = 90.12^\circ$) is visible at $2\theta = 48.0^\circ$. In contrast, the (002) cubic peak for MgO (space group $Fm\bar{3}m$, $a = 4.212 \text{ \AA}$) is at 42.9° . The weaker peaks around $2\theta = 46^\circ$ originate from a rhombohedral-like phase in the epitaxial films, while the peak at $2\theta = 38.5^\circ$ indicates the tetragonal-like phase.²⁰

Reciprocal space maps (RSMs) of diffraction peaks close to the substrate’s pseudocubic directions were utilized to obtain a component of the films’ periodicity in the plane, as shown by the examples in Figs. 2(a) and 2(b) close to the $(103)_c$ substrate peak for LaAlO_3 . For a 552-nm-thick layer of BDFO/L the film can be seen to be predominantly relaxed towards a bulk-like phase, as the in-plane component q_x of the scattering vector does not match that of the substrate [Fig. 2(a)]. Conversely, RSMs for the tetragonal-like (T-like) films indicated that no in-plane relaxation occurred (q_x the same for epitaxial film and substrate), as shown in Fig. 2(b).

A rhombohedral cell (space group $R3c$) provided a good fit for the BDFO and BLDFO films, where the observed diffraction peaks lay close to the values for bulk BFO. Fits were obtained by calculating 2θ positions for various peaks [e.g., (110), (220), (330), (431), (442) in the rhombohedral setting] using the two free parameters (a and α) and finding the best fit to experiment graphically via a contour plot of the error. The unit-cell parameters thus obtained were slightly smaller than bulk BFO,² which has $a = 5.63 \text{ \AA}$, $\alpha = 59.4^\circ$ and are summarized in Table I. The tetragonal distortion to the pseudocubic cell was small for the rare-earth-doped films, at $c/a < 1.01$ for BDFO and BLDFO. Two different undoped BFO films were explored: one with a weak tetragonal distortion $c/a = 1.03$ that was primarily rhombohedral (R-BFO, $a = 5.617 \text{ \AA}$, $\alpha = 58.7^\circ$), and a film with enhanced tetragonality $c/a = 1.23$ (T-BFO, $c = 4.68 \text{ \AA}$, $a = 3.789 \text{ \AA}$).

B. Ellipsometry and DFT

The complex refractive index $\tilde{n} = n + ik$ of the films was characterized using variable-angle spectroscopic ellipsometry. The R-BFO and T-BFO films were found to have similar \tilde{n} to those previously reported²¹ and were parameterized using a series of Tauc-Lorentz oscillators. \tilde{n} is reported in Figs. 3(a) and 3(c) for R-BFO and BDFO. Substitution with Dy was found to reduce n in comparison to R-BFO and to decrease the band gap slightly.

First-principles calculations of \tilde{n} were performed for our experimental BFO cell dimensions using the LSDA + U approach and the Kubo-Greenwood formalism.^{22,23} A good match between simulation [dashed lines in Fig. 3(a)] and experiment for BFO was obtained with a Hubbard $U = 6 \text{ eV}$ for Fe $3d$ electrons. The site-resolved density of states around the optical gap is shown in Fig. 3(b), where the chemical potential is at zero energy. The highest valence band is a mixture of O $2p$ states and the Bi $6s$ lone pair responsible for ferroelectricity, while the lowest conduction band is predominantly Fe $3d$ in character, with some Bi $6p$ hybridization.

To attempt to model the optical properties of BDFO, the experimental unit cell ($a = 5.535 \text{ \AA}$, $\alpha = 59.1^\circ$) was doubled in one dimension. One of the four Bi atoms was substituted by Dy to allow a simulation of $\text{Bi}_{0.75}\text{Dy}_{0.25}\text{FeO}_3$,

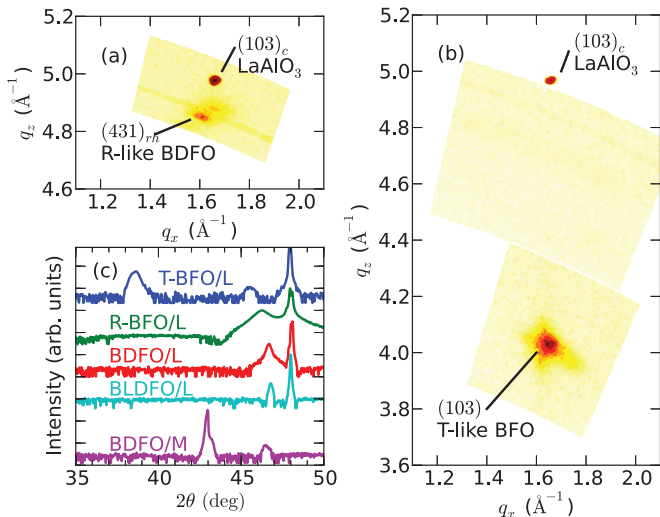


FIG. 2. (Color online) (a) Reciprocal space map (RSM) around the $(103)_c$ substrate peak for R-like BDFO/L. (b) RSM around the $(103)_c$ substrate peak for T-like BFO/L. (c) ω - 2θ x-ray diffraction scans for (from top to bottom) T-like BiFeO_3 (300 nm), R-like BiFeO_3 (300 nm), $\text{Bi}_{0.7}\text{Dy}_{0.3}\text{FeO}_3$ (552 nm) and $\text{Bi}_{0.6}\text{La}_{0.1}\text{Dy}_{0.3}\text{FeO}_3$ (323 nm) on LaAlO_3 , and $\text{Bi}_{0.7}\text{Dy}_{0.3}\text{FeO}_3$ (397 nm) on MgO .

TABLE I. Summary of structural parameters and elastic moduli of BiFeO₃. Here V_0 denotes the volume per atom, the complex refractive index is \tilde{n} , and the acoustic phonon frequency is f . Subscripts R , T , and C refer to the rhombohedral, tetragonal, and cubic unit vectors, respectively.

| Material (label) | Unit cell | V_0 (Å ³) | \tilde{n} at 800 nm (400 nm) | f (GHz) | Propagation direction | Elastic modulus (GPa) | Reference |
|--|--|-------------------------|--------------------------------------|-----------|-----------------------|-----------------------|-----------|
| BiFeO ₃ on LaAlO ₃ (R-BFO/L) | Rhombohedral, $a = 5.617$ Å, $\alpha = 58.7^\circ$ | 12.16 | $2.80 + 0.02i$ ($3.46 + 0.74i$) | 24 | [001] _C | 100 | This work |
| Bi _{0.7} Dy _{0.3} FeO ₃ (BDFO/L) | Rhombohedral, $a = 5.515$ Å, $\alpha = 59.6^\circ$ | 11.71 | $2.57 + 0.02i$ ($2.85 + 0.32i$) | 34 | [001] _C | 237 | This work |
| Bi _{0.6} La _{0.1} Dy _{0.3} FeO ₃ (BLDFO/L) | Rhombohedral, $a = 5.493$ Å, $\alpha = 59.7^\circ$ | 11.65 | $2.48 + 0.00i$ ($2.67 + 0.33i$) | 32 | [001] _C | 222 | This work |
| Bulk BiFeO ₃ | Rhombohedral, $a = 5.63$ Å, $\alpha = 59.4^\circ$ | 12.46 | 2.8 | 36.0 | [010] _R | 221 | Ref. 27 |
| BiFeO ₃ on SrTiO ₃ | Rhombohedral, $a = 5.63$ Å, $\alpha = 59.4^\circ$ | 12.46 | 2.8 | 34.2 | [010] _R | 200 | Ref. 29 |
| BiFeO ₃ , theory, $U = 0$ eV | Rhombohedral | 12.46 | | | [010] _R | 137 | Ref. 35 |
| BiFeO ₃ , theory, $U = 0$ eV | Rhombohedral | 12.16 | | | [001] _C | 161 | Ref. 35 |
| BiFeO ₃ , theory, $U = 0$ eV | Rhombohedral | 11.7 | | | [001] _C | 180 | Ref. 35 |
| BiFeO ₃ on LaAlO ₃ (T-BFO/L) | Tetragonal, $c/a = 1.23$ $c = 4.658$ Å, $a = 3.789$ Å | 13.38 | 2.47 | 25 | [001] _T | 127 | This work |
| BiFeO ₃ , theory, $U = 4$ eV | Tetragonal, $c/a = 1.28$ $c = 4.786$ Å, $a = 3.739$ Å | 13.38 | | | [001] _T | 100 | Ref. 36 |

close to the experimental Dy doping level of 30%. For dysprosium, a twenty-electron valence orbital basis set was used ($5s^25p^64f^{10}6s^25d^0$), with $U = 6$ eV for the $4f$ electrons. While the simulated Dy magnetic moment in BDFO was $5.06\mu_B$, in reasonable agreement with experiment ($5.87\mu_B$ for DyFeO₃, Ref. 24), the optical properties are in much poorer accord with experiment, as Fig. 3(c) indicates. This

may be due in part to neglecting spin-orbit interactions in the DFT calculations,^{22,23} which are particularly important for Dy. The degree of convergence was also poorer than for a BFO supercell without Dy, as reported previously.²⁵ The simulated density of states for BDFO demonstrates a hybridization between the Fe $3d$ and Dy $4f$ orbitals, with a Fe $3d$ band appearing within the band gap of BFO that lowers the calculated band gap. Experimentally, this reduction is less pronounced, as evidenced by Fig. 3(c).

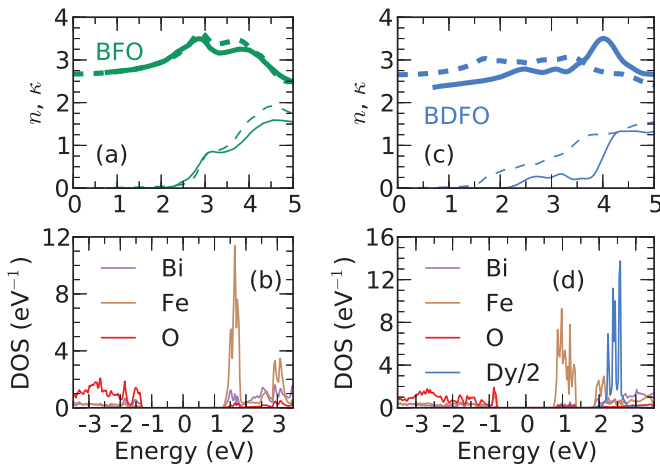


FIG. 3. (Color online) (a) Complex refractive index $\tilde{n} = n + i\kappa$ of R-BFO from ellipsometry (thick green line: n , thin green line: κ) is in close agreement with first-principles calculation (dashed lines, see text). (b) Atomic density of states (DOS) for R-BFO, from calculation. Panels (c) and (d) show that n and κ for BDFO (blue lines, from ellipsometry) are suppressed in the range 0–5 eV in comparison with R-BFO. The density of states for Dy has been scaled down by a factor of two.

III. TIME-RESOLVED REFLECTIVITY

The fundamental beam from a mode-locked Ti:sapphire laser oscillator (4 MHz, 650 nJ, 50 fs) was doubled in frequency to 400 nm (3.1 eV) to photoexcite the multiferroic films at a fluence of $60 \mu\text{J}/\text{cm}^2$. The transient optical reflectivity subsequent to excitation was detected using a time-delayed fraction of the fundamental beam (800 nm or 1.55 eV), which was incident on the sample at close to normal incidence [i.e., along [001] in the pseudocubic representation, see Fig. 1]. The absorption depth of the samples for the pump and probe are $\delta(400 \text{ nm}) = 40\text{--}100 \text{ nm}$ and $\delta(800 \text{ nm}) = 1.5 \mu\text{m}$.

The time-resolved reflectivity of the R-BiFeO₃/LaAlO₃ film is shown in Fig. 4(a), under photoexcitation at 3.1 eV. The sharp rise at zero time corresponds to the rapid transfer of electrons from the hybridized O $2p$ /Bi $6s$ valence band to the Fe $3d$ /Bi $6p$ conduction band. A similar rapid rise and decay in reflectivity has been reported in recent studies of bulk BFO^{26,27} and thin films of BFO grown on SrTiO₃^{28,29} and YSZ.²⁸ The nonexponential decay can be attributed to two timescales for electronic relaxation, initially via optical phonon emission as in III-V semiconductors.³⁰ The slower recovery could

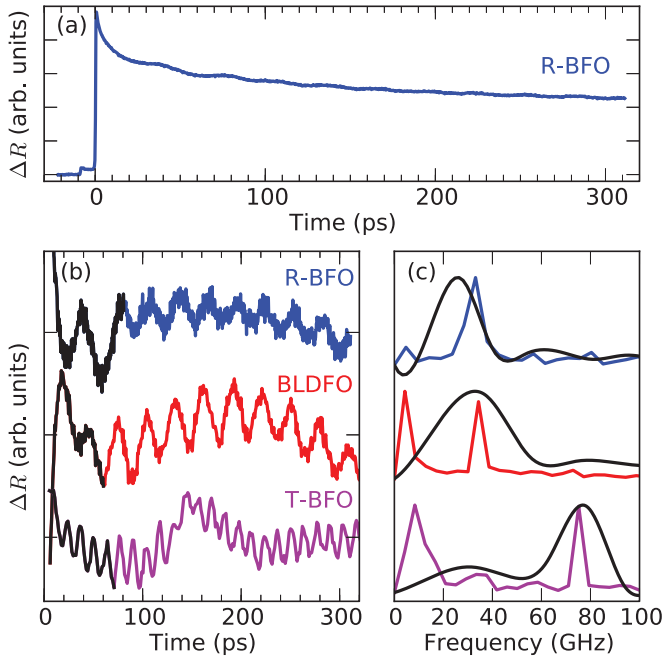


FIG. 4. (Color online) (a) Time-resolved reflectivity of R-BFO film on LaAlO₃. Coherent oscillations in the reflectance are shown in the (b) time and (c) frequency domains after subtraction of the electronic response, for R-BFO (top, blue), BLDFO (middle, red), and T-BFO (bottom, purple) films on LaAlO₃. Spectra are shown normalized to their maximum values. At early times (black) the acoustic phonon pulse is within the film, while at later times (colored) the acoustic pulse propagates through the substrate (Sec. IV). The T-BFO films exhibit a strong oscillation at 75 GHz, attributed to a magnon (Sec. V).

result from incoherent acoustic phonon emission, spin-lattice coupling,²⁸ or radiative recombination.²⁶

A distinct oscillation can be seen superimposed on the reflectivity transient in Fig. 4(a). The background quasistatic component was removed numerically in order to examine the oscillation, as shown in Fig. 4(b) for R-BFO (top), BLDFO (middle), and T-BFO (bottom) in the time-domain. The corresponding frequency-domain spectra (normalized) are given in Fig. 4(c). While the R-BFO and BLDFO datasets are dominated by low-frequency oscillations, the T-BFO data exhibit a higher-frequency oscillation. The following sections discuss the low-frequency modes, which originate from acoustic phonons, and the high-frequency mode, which can be assigned to a magnon.

Since the reflectivity of a sample at normal incidence is $R = |(\tilde{n} - 1)/(\tilde{n} + 1)|^2$, the photoinduced change ΔR will be proportional to the change in the refractive index. Oscillations in ΔR can therefore arise from periodic changes to the refractive index, as created by acoustic phonon modes in BFO^{27,29} and LuMnO₃.^{31,32} Alternatively, since $\tilde{n} = \sqrt{\epsilon\mu}$ (where ϵ and μ are the dielectric function and permeability, respectively), magnon modes can modulate ΔR , as reported⁹ for the hexaferrite Ba_{0.5}Sr_{1.5}Zn₂Fe₁₂O₂₂. As discussed in detail below, the two mechanisms can be distinguished by their time dependence, the variation of the mode frequency with

probe wavelength, and the influence of magnetic field and temperature.

IV. ELASTIC MODULI AND ACOUSTIC PHONONS

A. Acoustic phonon contribution to reflectivity change

A strain pulse is created by the perturbation of the lattice by photoexcitation, and propagates through the multiferroic film. The oscillation arises from interference between the fraction of the probe pulse specularly reflected from the sample surface and the fraction reflected from the propagating strain pulse.³³ This mechanism can also be described as stimulated Brillouin scattering.³⁴ The strain pulse results in a characteristic frequency $f = 2nv/\lambda$ for the oscillation in ΔR (Ref. 33), where v is the longitudinal acoustic phonon speed and the refractive index n is evaluated at the probe wavelength λ . As such, on entering the substrate f will change as a result of a different n and v . For the R-BFO film this change in period is evident at 80 ps in Fig. 4(b). The frequency-domain analysis in Fig. 4(c) has been time windowed to take this into account, with black lines showing early times, where the mode is in the film, and colored lines corresponding to later times, when the mode has propagated into the substrate. Time-domain fits (not shown) were also utilized to determine oscillation frequencies, particularly for early times.

B. Elastic properties of anisotropic BiFeO₃

In anisotropic media Hooke's law is written $X_{ij} = c_{ijkl}x_{kl}$, where the stress X_{ij} and strain x_{ij} are second-rank tensors linked by the fourth-rank elastic modulus tensor c_{ijkl} . Symmetry and energy arguments^{35,37} permit the reduction of c_{ijkl} to a 6×6 matrix \mathbf{c} , which can be linked to the acoustic wave speed v_{ij} and density ρ via $c_{ij} = \rho v_{ij}^2$ (Voigt notation). The elastic matrices are as follows for cubic (C), tetragonal (T), and rhombohedral (R) phases:

$$\mathbf{c}^C = \begin{pmatrix} c_{11} & c_{12} & c_{12} & 0 & 0 & 0 \\ c_{12} & c_{11} & c_{12} & 0 & 0 & 0 \\ c_{12} & c_{12} & c_{11} & 0 & 0 & 0 \\ 0 & 0 & 0 & c_{44} & 0 & 0 \\ 0 & 0 & 0 & 0 & c_{44} & 0 \\ 0 & 0 & 0 & 0 & 0 & c_{44} \end{pmatrix}, \quad (1)$$

$$\mathbf{c}^T = \begin{pmatrix} c_{11} & c_{12} & c_{13} & 0 & 0 & 0 \\ c_{12} & c_{11} & c_{13} & 0 & 0 & 0 \\ c_{13} & c_{13} & c_{33} & 0 & 0 & 0 \\ 0 & 0 & 0 & c_{44} & 0 & 0 \\ 0 & 0 & 0 & 0 & c_{44} & 0 \\ 0 & 0 & 0 & 0 & 0 & c_{66} \end{pmatrix}, \quad (2)$$

$$\mathbf{c}^R = \begin{pmatrix} c_{11} & c_{12} & c_{13} & c_{14} & 0 & 0 \\ c_{12} & c_{11} & c_{13} & -c_{14} & 0 & 0 \\ c_{13} & c_{13} & c_{33} & 0 & 0 & 0 \\ c_{14} & -c_{14} & 0 & c_{44} & 0 & 0 \\ 0 & 0 & 0 & 0 & c_{44} & c_{14} \\ 0 & 0 & 0 & 0 & c_{14} & (c_{11} - c_{12})/2 \end{pmatrix}, \quad (3)$$

where the point groups $3m$ and $4mm$ were assumed for the rhombohedral and tetragonal phases, respectively. Here, the matrix subscripts are a shorthand notation for the tensor

subscripts, defined as $1 = 11, 2 = 22, 3 = 33, 4 = 23, 5 = 31$, and $6 = 12$. A tetragonal distortion along [001] will alter c_{33} without changing $c_{11} = c_{22}$ and will tend to reduce the elastic constant such that $c_{33}^T < c_{11}^C$. Similarly, a rhombohedral expansion along [111] lowers the elastic constant in this direction; $c_{33}^R < c_{11}^C$.

Assuming a pseudocubic [001]-oriented crystal, the almost-collinear photoexcitation and probe beams of the experimental geometry allow $c_{11}^C = c_{1111}^C$ to be determined; namely, the elastic modulus for stress and strain along the pseudocubic [001] direction. For a tetragonal crystal the experiment probes c_{33}^T along the direction of the tetragonal distortion (z axis). The case of a rhombohedral crystal is more complex: the elastic matrix as written in Eq. (3) uses a Cartesian coordinate system x', y', z' defined with z' parallel to the [111] rhombohedral direction, y' parallel to a projection of a unit vector of the rhombohedral cell into the plane normal to z' , and x' completing the orthogonal set.³⁸ These coordinate systems are defined in Fig. 1, along with the alternative description of the rhombohedral phase in the trigonal setting.

C. Results and discussion

In order to separate the acoustic phonon contributions from the film and substrate ΔR datasets must be time windowed, as discussed in Sec. IV A and illustrated in Fig. 4(b). For R-BFO, the Fourier spectra of the time-windowed ΔR oscillation in Fig. 4(c) reveal a frequency $f = 24$ GHz and $f = 33.7 \pm 0.5$ GHz at early and late times, respectively. The oscillation frequency in the LaAlO₃ substrate yields $v = 6740 \pm 100$ ms⁻¹ using $n(800 \text{ nm}) = 2.0$, and thus $c_{11} = 296 \pm 6$ GPa, corresponding well with $c_{11} = 290$ GPa for LA phonons propagating along [001] reported in Ref. 39. An oscillation at the same frequency can be seen at late times in all samples on LaAlO₃, as the spectra in Fig. 4(c) indicate. However, variations in the substrate's acoustic mode amplitude and/or frequency are discernible between different LaAlO₃ substrates [Fig. 4(c)] and the same substrate for varying magnetic field or temperature (Figs. 5 and 6). A possible explanation is the existence of birefringent twin domains⁴⁰ in LaAlO₃, which have an extent of 10–100 μm , comparable to the size of the focused probe beam. Probing multiple or different twin domains with varying orientation and refractive index may alter the amplitude and/or frequency of the substrate mode. Lower-frequency oscillations (<20 GHz) discernible in these figures may indicate a contribution from substrate TA phonon modes (with lower elastic constants) to the time-resolved reflectivity,²⁷ or may be artifacts from the finite length of the time-domain scans (around 300 ps).

The elastic moduli for the films were determined from the acoustic-mode frequencies (>20 GHz) and are summarized in Table I together with the structural parameters. The measured elastic constants range from 100–237 GPa, and depend on composition and crystal structure, as discussed below.

Time-resolved reflectivity has been used previously to determine the elastic constants of bulk single-crystal BFO and bulk-like BiFeO₃ on SrTiO₃ along [101]-oriented crystals (rhombohedral [010] direction),^{27,29} and these results are also included in Table I. Conventional ultrasound measurements

yielded 127 GPa for polycrystalline BFO,⁴¹ substantially lower because of averaging over all crystallographic directions.

First-principles calculations of \mathbf{c}^R using DFT (within the GGA + U approach, with various values of the Hubbard constant $U = 0$ –6 eV) have been reported in Ref. 35, while Ref. 36 discussed similar calculations for \mathbf{c}^T . To compare the theoretical values of \mathbf{c}^R with experiment a conversion was made from the Cartesian coordinate system used in the first-principles calculations,³⁵ which has z' oriented along the three-fold [111] axis, to the experimental geometry with z along the pseudocubic [001] direction. This was achieved using the transformation matrix α and the expression

$$\mathbf{c} = \alpha^{-1} \mathbf{c}' \alpha^{-1}, \quad (4)$$

which is derived in textbooks describing the elastic properties of anisotropic media; e.g., Ref. 37. A similar transformation was performed to allow the elastic constant in the [010]_R direction, as reported in Refs. 27 and 29, to be compared with the values of \mathbf{c}^R derived from DFT. Since \mathbf{c}^R and \mathbf{c}^T are sensitive functions of the unit-cell volume, with larger cells exhibiting lower diagonal components c_{ii} in the elastic modulus tensor, the theoretical predictions at the same unit-cell volume as experiment were adopted.

Several trends are apparent in the data reported in Table I. Within the rhombohedral phase smaller unit-cell volumes correspond to higher elastic constants. In the experimental tetragonal phase ($c/a = 1.23$) $c_{33} = 160$ GPa is reduced in comparison to the majority of rhombohedral-phase results. This is in reasonable accord with DFT calculations,³⁶ which predict $c_{33} = 100$ GPa for a larger $c/a = 1.28$.

V. MAGNON RESONANCE

In the pristine rhombohedral-phase samples (R-BFO, BDFO, BLDFO) only acoustic modes (below 50 GHz) can be observed, as evidenced by Fig. 4(b). In contrast, the tetragonal-phase sample (T-BFO) exhibits an additional oscillation at a higher frequency, 75 GHz. In this section this mode is discussed in detail with respect to its structural, magnetic-field, and temperature dependence. These findings allow the mode to be identified as a magnon originating from the coherent oscillation of weak ferromagnetic order in the multiferroic film. Following the experimental results a discussion of the origin of the magnon mode is given in Sec. V D.

A. Magnetic-field dependence

A static magnetic field $B \leq 0.5$ T was applied in the growth direction. For both rhombohedral BDFO and BLDFO a mode emerged upon magnetization similar to that observed for pristine tetragonal BFO, as demonstrated for BLDFO in Fig. 5. The onset of the magnon mode appears to correlate with the field required to saturate the magnetization. For a pristine sample of BDFO (i.e., one not previously exposed to a magnetic field) the 75 GHz mode appeared at $B \gtrsim 0.45$ T, while for BLDFO $B \gtrsim 0.3$ T was sufficient to produce this mode. This is in agreement with the slightly lower saturation field of BLDFO (~ 0.36 T) compared to BDFO (~ 0.64 T).¹⁹ The mode can be identified as originating from a weak permanent magnetic moment as after the removal of the

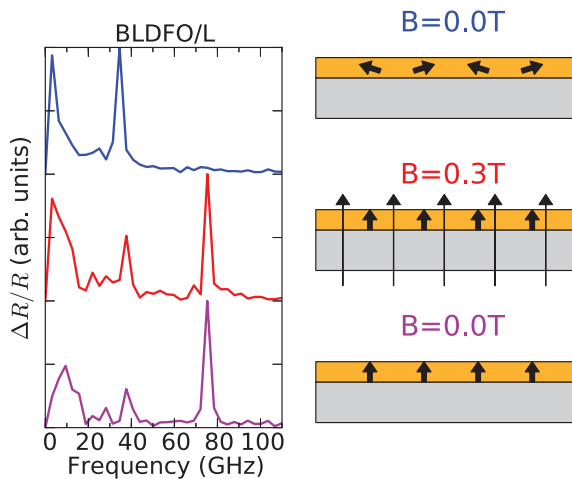


FIG. 5. (Color online) Influence of a magnetic field upon ΔR spectra for BLDFO (323 nm thick) on LaAlO_3 . Here the time-domain data was over the range from 15–332 ps, during which the acoustic pulse was in the film and then the substrate. For a pristine sample (top blue line), not previously exposed to a magnetic field, only acoustic phonon oscillations are evident. Under a magnetic field $B = 0.3$ T in the growth direction an additional oscillation at 75 GHz can be witnessed (middle red line), which is assigned to a magnon mode. After the removal of the magnetic field (bottom purple line) the magnon resonance remains. The diagrams (right) indicate the magnetic-domain structure at each stage.

magnetic field the mode remains present (bottom curve in Fig. 5) and appears to persist indefinitely.

For a magnon in a simple antiferromagnet or ferromagnet an increase in frequency with applied magnetic field would be expected.⁴² No shift in the frequency of the magnon mode was observed with magnetic field in the range examined ($B \leq 0.5$ T). This may be a consequence of the relatively weak magnetic field applied in comparison with the large values (20 T) required to suppress the spin cycloid of BFO.¹⁶ Coherent magnons in the multiferroic $\text{Ba}_{0.6}\text{Sr}_{1.4}\text{Zn}_2\text{Fe}_{12}\text{O}_{22}$ also do not change in frequency under similar applied fields.⁹

B. Temperature dependence

The temperature dependence of the 75 GHz magnon mode was also examined. Figure 6 presents the time-resolved reflectivity spectra for the T-BFO phase (where the 75 GHz mode is intrinsic) for 20 °C, 200 °C, 320 °C and after being returned to 20 °C. Both the amplitude and the frequency of the magnon modes of simple ferromagnets and antiferromagnets are highly temperature dependent, with the intensity of mode being expected to drop to zero as the Néel temperature T_N is approached. By 200 °C the magnitude of the 75 GHz mode has reduced in comparison to that at 20 °C, while at 320 °C the mode is no longer discernible. This latter temperature is 50 °C below the $T_N = 643$ K (370 °C) for bulk BiFeO_3 , indicating that the magnon is linked to the AFM sublattice order, from which the weak ferromagnetic component arises via the DM interaction.

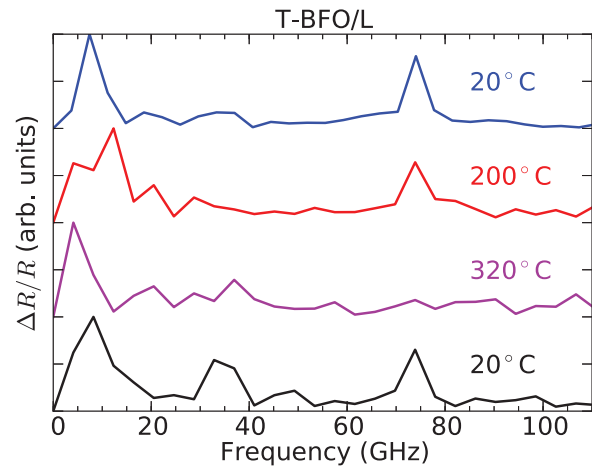


FIG. 6. (Color online) ΔR spectra for T-BFO at sample temperatures (from top to bottom) of 20 °C (blue), 200 °C (red), 320 °C (purple), and on subsequent cooling to 20 °C (black). The 75 GHz mode disappears as the temperature approaches the Néel temperature and reappears upon cooling. The time-domain data were windowed from 90–340 ps (acoustic pulse in substrate).

C. Additional results

Additional factors point to a magnon, rather than an acoustic phonon, as the origin of the 75 GHz mode observed in pristine T-BFO and magnetized rhombohedral BFO and BLDFO. The mode is present through the time windows examined. This persistence throughout the entire time window rules out an acoustic mode: as discussed in Sec. IV, the acoustic oscillation in the substrate is at $f = 33.7$ GHz.

As discussed in Sec. IV A, the observed frequency for a phonon mode measured by time-resolved reflectivity would be expected to display a $1/\lambda$ dependence. The wavelength dependence of the 75 GHz oscillation was therefore investigated using spectrally narrowed probe beams around 810 and 785 nm. This difference would be expected to give a frequency shift of ~ 3 GHz for a phonon mode at ~ 75 GHz. No shift in the high-frequency mode was observed, and the substrate acoustic mode (at late times) was observed to shift as expected.

D. Magnon resonance: discussion

The coherent magnon mode was observed for both tetragonal phase BFO and Dy-doped BFO and cannot therefore arise from the precession of Dy moments. Rather, the Fe sites provide the relevant magnetic sublattices. A possible microscopic mechanism for the observed ultrafast stimulation of the magnetic permeability μ is as follows: UV photoexcitation transfers an electron from an oxygen $2p$ orbital to an iron $3d$ state (Fig. 3), altering the electronic configuration from high-spin $3d^5$ (Fe^{3+}) to the low-spin $3d^6$ (Fe^{2+}) state. This impulsive change in μ then alters the reflectivity.

Interestingly, while the magnon is present intrinsically in the tetragonal-phase sample, magnetization was required to create it in the rhombohedral-phase rare-earth-doped films. This suggests that the break in symmetry along the growth direction introduced by the tetragonal distortion produces an effect similar to that of the application of a low magnetic field. The magnon frequency is comparable for both T-BFO and

rare-earth-doped R-BFO, which may be a result of the similar in-plane lattice constants of all the samples investigated and indicates a similar magnetic structure. A study of the magnetic domains of the weak ferromagnetic moment (for instance using magnetic force microscopy) is necessary to further investigate whether the tetragonal distortion can result in a spontaneous local moment. The size of the magnetic domains is also highly relevant: to observe a coherent magnon signal the domain size must be larger than the spot size of the infrared probe ($\sim 10 \mu\text{m}$).

In contrast to the single-magnon mode reported herein, a sequence of magnon modes separated by 7.5 cm^{-1} (225 GHz) is seen in inelastic (Raman) scattering on bulk BFO.⁸ No magnons have been reported in bulk R-BFO and thin-film R-BFO with time-resolved reflectivity spectroscopy.^{27,29} Note that a previous report⁴³ of a magnon at 46 GHz in thin-film BFO corresponds to the acoustic phonon mode of the SrTiO₃ substrate.⁴⁴ In comparison with the magnon-induced ΔR oscillations in a hexaferrite⁹ at 40 GHz (0.17 meV), the magnons reported herein for T-BFO and BLDFO are long lived (lifetime above 1 ns) and are observed above room temperature.

In thin-film rhombohedral BFO the magnon response was investigated theoretically by solving the Landau-Lifshitz equations for two AFM sublattices coupled by the DM interaction.⁴⁵ For thin-film BFO two modes at ~ 1.3 GHz and 8 GHz were predicted, with the high-frequency mode (where sublattices oscillate out of phase) corresponding to the DM interaction strength D_{ij} .⁴⁵ While these modes are below our experimental resolution, an enhanced DM interaction may increase the frequency of these magnon modes, creating the 75 GHz magnon-induced ΔR oscillation. The predicted anisotropy of the magnon dispersion may be used to discriminate between the two predicted modes.⁴⁵ The

low-frequency mode is more anisotropic, whereas no change in the frequency of the magnon in T-BFO or BDFO was seen upon rotating the sample about the surface normal. This suggests that the magnon reported here corresponds to the more isotropic out-of-phase mode,⁴⁵ and that the observed mode at 75 GHz corresponds to a DM interaction strength $D_{ij} = 0.31 \text{ meV}$. This is enhanced in comparison with the value of $D_{ij} = 0.16 \text{ meV}$ recently reported for bulk rhombohedral BFO.⁴⁶

VI. CONCLUSION

In conclusion, the dynamics of coherent magnons and acoustic phonons in multiferroic thin films of tetragonal and rare-earth-doped BiFeO₃ were investigated using time-resolved reflectivity. Oscillations in the reflectivity were attributed to dynamic modulations of the refractive index by acoustic phonons and magnons. The creation of a magnon mode after magnetization or using tetragonal BiFeO₃ provide promising routes to create a magnetoelectric multiferroic with a tailored magnonic response. The temperature and magnetic-field dependence of the magnon resonance allowed it to be assigned to a ferromagnetic moment linked to antiferromagnetic order by the Dzyaloshinskii-Moriya interaction. In addition, the ultrafast photoacoustic technique utilized in this work allows direct experimental access to the elastic moduli of ferroic thin films, which can be hard to characterize using traditional transducer-based methods.

ACKNOWLEDGMENTS

The authors would like to thank J. Alexander-Webber for performing AFM measurements, the EPSRC (UK) for financial support, and J. A. Woollam and the National Physical Laboratory (UK) for the use of a spectroscopic ellipsometer.

*j.lloyd-hughes@warwick.ac.uk

¹T. Kimura, T. Goto, H. Shintani, K. Ishizaka, T. Arima, and Y. Tokura, *Nature (London)* **426**, 55 (2003).

²J. Wang, J. B. Neaton, H. Zheng, V. Nagarajan, S. B. Ogale, B. Liu, D. Viehland, V. Vaithyanathan, D. G. Schlom, U. V. Waghmare *et al.*, *Science* **299**, 1719 (2003).

³N. A. Spaldin and M. Fiebig, *Science* **309**, 391 (2005).

⁴R. Ramesh and N. A. Spaldin, *Nat. Mater.* **6**, 21 (2007).

⁵M. Bibes and A. Barthelemy, *Nat. Mater.* **7**, 425 (2008).

⁶H. Katsura, A. V. Balatsky, and N. Nagaosa, *Phys. Rev. Lett.* **98**, 027203 (2007).

⁷S. W. Cheong and M. Mostovoy, *Nat. Mater.* **6**, 13 (2007).

⁸M. Cazayous, Y. Gallais, A. Sacuto, R. de Sousa, D. Lebeugle, and D. Colson, *Phys. Rev. Lett.* **101**, 037601 (2008).

⁹D. Talbayev, S. A. Trugman, A. V. Balatsky, T. Kimura, A. J. Taylor, and R. D. Averitt, *Phys. Rev. Lett.* **101**, 097603 (2008).

¹⁰N. Kida, Y. Takahashi, J. S. Lee, R. Shimano, Y. Yamasaki, Y. Kaneko, S. Miyahara, N. Furukawa, T. Arima, and Y. Tokura, *J. Opt. Soc. Am. B* **26**, A35 (2009).

¹¹P. Rovillain, R. de Sousa, Y. Gallais, A. Sacuto, M. A. Measson, D. Colson, A. Forget, M. Bibes, A. Barthelemy, and M. Cazayous, *Nat. Mater.* **9**, 975 (2010).

¹²D. Talbayev, S. A. Trugman, S. Lee, H. T. Yi, S. W. Cheong, and A. J. Taylor, *Phys. Rev. B* **83**, 094403 (2011).

¹³G. Catalan and J. Scott, *Adv. Mater.* **21**, 2463 (2009).

¹⁴C. Ederer and N. A. Spaldin, *Phys. Rev. B* **71**, 060401 (2005).

¹⁵I. Sosnowska, T. Peterlinneumaier, and E. Steichele, *J. Phys. C: Solid State Phys.* **15**, 4835 (1982).

¹⁶Y. F. Popov, A. M. Kadomtseva, S. S. Krotov, D. V. Belov, G. P. Vorob'ev, P. N. Makhov, and A. K. Zvezdin, *Low Temp. Phys.* **27**, 478 (2001).

¹⁷V. R. Palkar, R. Anisha, R. Pinto, and S. Bhattacharya, *J. Mater. Res.* **22**, 2068 (2007).

¹⁸P. K. Petrov, V. R. Palkar, A. K. Tagantsev, H. I. Chien, K. Prashanthi, A. K. Axelsson, S. Bhattacharya, and N. M. Alford, *J. Mater. Res.* **22**, 2179 (2007).

¹⁹K. Prashanthi, B. A. Chalke, K. C. Barick, A. Das, I. Dhiman, and V. R. Palkar, *Solid State Commun.* **149**, 188 (2009).

²⁰H. M. Christen, J. H. Nam, H. S. Kim, A. J. Hatt, and N. A. Spaldin, *Phys. Rev. B* **83**, 144107 (2011).

²¹P. Chen, N. J. Podraza, X. S. Xu, A. Melville, E. Vlahos, V. Gopalan, R. Ramesh, D. G. Schlom, and J. L. Musfeldt, *Appl. Phys. Lett.* **96**, 131907 (2010).

- ²²Atomistix toolkit version 12.2.2, quantumwise a/s, <http://www.quantumwise.com>.
- ²³J. M. Soler, E. Artacho, J. D. Gale, A. Garcia, J. Junquera, P. Ordejon, and D. Sanchez-portal, *J. Phys.: Condes. Matter* **14**, 2745 (2002).
- ²⁴Y. Du, Z. X. Cheng, X. L. Wang, and S. X. Dou, *J. Appl. Phys.* **107**, 09D908 (2010).
- ²⁵L. Chen, T. Li, S. Cao, S. Yuan, F. Hong, and J. Zhang, *J. Appl. Phys.* **111**, 103905 (2012).
- ²⁶Y. M. Sheu, S. A. Trugman, Y. Park, S. Lee, H. T. Yi, S. Cheong, Q. X. Jia, A. J. Taylor, and R. P. Prasankumar, *Appl. Phys. Lett.* **100**, 242904 (2012).
- ²⁷P. Ruello, T. Pezeril, S. Avanesyan, G. Vaudel, V. Gusev, I. C. Infante, and B. Dkhil, *Appl. Phys. Lett.* **100**, 212906 (2012).
- ²⁸Z. M. Jin, Y. Xu, Z. B. Zhang, G. F. Li, X. Lin, G. H. Ma, Z. X. Cheng, and X. L. Wang, *Appl. Phys. Lett.* **100**, 071105 (2012).
- ²⁹L. Y. Chen, J. C. Yang, C. W. Luo, C. W. Laing, K. H. Wu, J. Lin, T. M. Uen, J. Y. Juang, Y. H. Chu, and T. Kobayashi, *Appl. Phys. Lett.* **101**, 041902 (2012).
- ³⁰J. Lloyd-Hughes, *Appl. Phys. Lett.* **100**, 122103 (2012).
- ³¹D. Lim, R. D. Averitt, J. Demsar, A. J. Taylor, N. Hur, and S. W. Cheong, *Appl. Phys. Lett.* **83**, 4800 (2003).
- ³²K. J. Jang, J. Lim, J. Ahn, J. H. Kim, K. J. Yee, J. S. Ahn, and S. W. Cheong, *New J. Phys.* **12**, 023017 (2010).
- ³³C. Thomsen, H. T. Grahn, H. J. Maris, and J. Tauc, *Phys. Rev. B* **34**, 4129 (1986).
- ³⁴S. Brivio, D. Polli, A. Crespi, R. Osellame, G. Cerullo, and R. Bertacco, *Appl. Phys. Lett.* **98**, 211907 (2011).
- ³⁵S. L. Shang, G. Sheng, Y. Wang, L. Q. Chen, and Z. K. Liu, *Phys. Rev. B* **80**, 052102 (2009).
- ³⁶H. Dong, C. Chen, S. Wang, W. Duan, and J. Li, *Appl. Phys. Lett.* **102**, 182905 (2013).
- ³⁷R. E. Newnham, *Properties of Materials: Anisotropy, Symmetry, Structure*, 1st ed. (Oxford University Press, Oxford, UK, 2005).
- ³⁸N. G. Pace and G. A. Saunders, *J. Phys. Chem. Solids* **32**, 1585 (1971).
- ³⁹M. A. Carpenter, S. V. Sinogeikin, J. D. Bass, D. L. Lakshtanov, and S. D. Jacobsen, *J. Phys.: Condes. Matter* **22**, 035403 (2010).
- ⁴⁰S. A. Hayward, F. D. Morrison, S. A. T. Redfern, E. K. H. Salje, J. F. Scott, K. S. Knight, S. Tarantino, A. M. Glazer, V. Shuvaeva, P. Daniel *et al.*, *Phys. Rev. B* **72**, 054110 (2005).
- ⁴¹E. P. Smirnova, A. Sotnikov, S. Ktitorov, N. Zaitseva, H. Schmidt, and M. Weihnacht, *Eur. Phys. J. B* **83**, 39 (2011).
- ⁴²J. van Kranendonk and J. van Vleck, *Rev. Mod. Phys.* **30**, 1 (1958).
- ⁴³L. Y. Chen, J. C. Yang, H. C. Shih, C. W. Liang, T. Y. Wu, S. K. Chou, C. W. Luo, K. H. Wu, Y. H. Chu, and T. Kobayashi, *J. Supercond. Novel Magn.* **24**, 731 (2011).
- ⁴⁴The LA-phonon speed of 7900ms^{-1} reported in Brivio *et al.* (Ref. 34) and a refractive index $n = 2.34$ at 800 nm results in an acoustic phonon frequency of 46 GHz, as reported in Chen *et al.* (Ref. 43).
- ⁴⁵R. de Sousa and J. E. Moore, *Appl. Phys. Lett.* **92**, 022514 (2008).
- ⁴⁶M. Matsuda, R. S. Fishman, T. Hong, C. H. Lee, T. Ushiyama, Y. Yanagisawa, Y. Tomioka, and T. Ito, *Phys. Rev. Lett.* **109**, 067205 (2012).